Stem Cell Reports
Article

ISSCR

OPEN ACCESS

Modeling Developmental and Tumorigenic Aspects of Trilateral Retinoblastoma via Human Embryonic Stem Cells

Yishai Avior,[1] Elyad Lezmi,[1] Dorit Yanuka,[1] and Nissim Benvenisty[1,*]
[1]The Azrieli Center for Stem Cells and Genetic Research, Institute of Life Sciences, The Hebrew University of Jerusalem, Givat-Ram, Jerusalem 91904, Israel
*Correspondence: nissimb@mail.huji.ac.il
http://dx.doi.org/10.1016/j.stemcr.2017.03.005

SUMMARY

Human embryonic stem cells (hESCs) provide a platform for studying human development and understanding mechanisms underlying diseases. Retinoblastoma-1 (*RB1*) is a key regulator of cell cycling, of which biallelic inactivation initiates retinoblastoma, the most common congenital intraocular malignancy. We developed a model to study the role of *RB1* in early development and tumor formation by generating *RB1*-null hESCs using CRISPR/Cas9. $RB1^{-/-}$ hESCs initiated extremely large teratomas, with neural expansions similar to those of trilateral retinoblastoma tumors, in which retinoblastoma is accompanied by intracranial neural tumors. Teratoma analysis further revealed a role for the transcription factor ZEB1 in RB1-mediated ectoderm differentiation. Furthermore, $RB1^{-/-}$ cells displayed mitochondrial dysfunction similar to poorly differentiated retinoblastomas. Screening more than 100 chemotherapies revealed an $RB1^{-/-}$-specific cell sensitivity to carboplatin, exploiting their mitochondrial dysfunction. Together, our work provides a human pluripotent cell model for retinoblastoma and sheds light on developmental and tumorigenic roles of *RB1*.

INTRODUCTION

Retinoblastoma is the most common primary intraocular pediatric cancer, with 95% of the cases diagnosed before 5 years of age (Kivela, 2009). Retinoblastoma is initiated by biallelic inactivation of the retinoblastoma 1 (*RB1*) gene. In heritable retinoblastoma, a primary germline mutation in *RB1* predisposes a child to retinal tumors, but only a second, somatic mutation in retinal cells initiates tumor growth (Goodrich, 2006). This heritable condition is responsible for all cases of bilateral retinoblastoma, i.e., involving tumors in both eyes (Dimaras et al., 2012; Richter et al., 2003). In up to 6% of patients, the inherited disease is manifested as trilateral retinoblastoma (TRb), where in addition to ocular tumors a primary neuroectodermal tumor also occurs (Dimaras et al., 2012).

RB1 encodes for the retinoblastoma protein (pRB), a tumor suppressor and a key regulator of cell cycle (Manning and Dyson, 2012). pRB was initially shown to regulate cell-cycle progression through binding of the transcriptional activator E2F transcription factor 1 (E2F1). pRB phosphorylation by cyclin-dependent kinases prevents this association, allowing cell-cycle progression (Dynlacht et al., 1994; Weinberg, 1995). However, it is now known that pRB binds numerous cofactors, and is involved in many cellular mechanisms such as apoptosis, genome stability maintenance, and differentiation (Benavente and Dyer, 2015; Burkhart and Sage, 2008; Dyson, 2016; Thomas et al., 2003). *Rb1*-deficient mouse embryos exhibit substantial developmental defects in mesenchymal development, bone formation, hematopoiesis, and the nervous system (Calo et al., 2010; Jacks et al., 1992). Conditional knockout mice revealed pRb roles in neural migration and neurogenesis during development and adulthood (Andrusiak et al., 2011; Ghanem et al., 2012). In humans, deletions in chromosome 13q including *RB1* were associated with brain abnormalities (Mitter et al., 2011; Rodjan et al., 2010), suggesting that it can play a role in human nervous system development.

While an inherited heterozygous mutation in *RB1* is the underlying cause of one-third of retinoblastoma cases, no cases of inherited homozygous inactivating mutations have been documented. Previous attempts to model retinoblastoma in mice were only partially successful, as *Rb1* ablation in mice is embryonic lethal, and *Rb1*-null chimeras do not recapitulate basic features of human retinoblastoma (Jacks et al., 1992). Other studies used mutations in additional murine genes alongside Rb1 to initiate retinoblastoma or model the role of *Rb1* in its initiation, diverging from its manifestation in humans (Classon and Harlow, 2002; Conklin et al., 2012).

Human embryonic stem cells (hESCs) are normal primary cells with an indefinite self-renewal capability and the potential to differentiate toward any cellular fate. These properties make hESCs extremely beneficial for the study of developmental processes and disease modeling (Avior et al., 2016). In addition, hESCs share cellular characteristics with cancer cells (Ben-David and Benvenisty, 2011), suggesting that they may also be useful in modeling tumorigenic diseases. We therefore chose hESCs as a platform to model biallelic *RB1* inactivation and TRb.

RESULTS

We used the CRISPR/Cas9 gene-editing approach to generate hESCs with mutations in *RB1*. Karyotypically

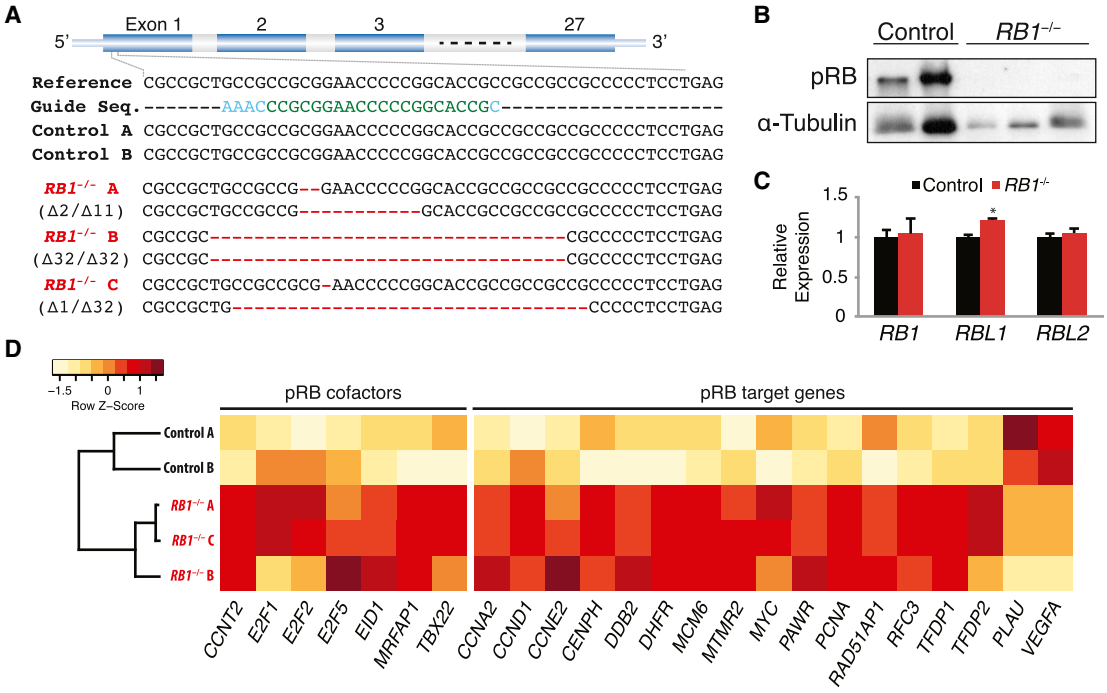

Figure 1. Generation and Characterization of *RB1*$^{-/-}$ hESCs

(A) DNA sequencing of control and mutant clones following CRISPR/Cas9 and a guide sequence targeting the first exon of the *RB1* gene (blue and green). Control A is the untreated cell line, and control B underwent the same transfection with a Cas9 vector without a guide sequence.

(B) Western blot analysis for pRB shows ablated protein expression in biallelic mutations in *RB1*.

(C) Relative gene expression of *RB1* homologs, *RBL1* and *RBL2*, in control and *RB1*$^{-/-}$ hESCs. Error bars represent SEM. *$p < 0.05$ (calculated using Student's t test).

(D) Heatmap of *RB1* cofactors and gene target expression. Two independent control cell lines and three mutant ones are shown.

See also Figure S1.

normal hESCs were transfected either with the *Cas9* gene alongside a guide RNA targeting the first exon of *RB1*, or with *Cas9* only as control. The integrity of *RB1* was then evaluated in individual clones using direct DNA sequencing, revealing two clones carrying a mutation in one allele (*RB1*$^{+/-}$) and three clones with mutations in both alleles (*RB1*$^{-/-}$) (Figures 1A and S1A). Western blot analysis validated the absence of pRB in the homozygous clones, whereas heterozygous clones maintained pRB expression as expected (Figures 1B and S1B). As pRB was previously shown to be important for chromosomal stability (Manning et al., 2010), genetic integrity of all clones was verified (Figure S1C).

To evaluate global gene expression patterns in the mutant cells, we performed RNA sequencing (RNA-seq) on control and the three *RB1*$^{-/-}$ clones. Of the expressed transcripts, 4.8% were either 2-fold upregulated or downregulated in the *RB1*$^{-/-}$ clones. In contrast to the absence of pRB due to frameshift mutations, the *RB1* transcript was not downregulated in the mutant clones (Figure 1C). However, *RB1*$^{-/-}$ clones exhibited a modest yet significant upregulation of the *RB1* homolog *RBL1* (but not *RBL2*), encompassing both redundancy and a possible compensation for pRB functional loss (Figure 1C). *RB1*$^{-/-}$ clones also showed upregulation of various pRB cofactors and immediate gene targets known to be repressed by pRB (Iwanaga et al., 2006; Prost et al., 2007; Stanelle et al., 2002; Vance et al., 2010), exhibiting downstream effects of *RB1* ablation (Figure 1D). Similarly, genes that are known to be upregulated by pRB binding to E2Fs, such as *PLAU* and *VEGFA* (Koziczak et al., 2000; Merdzhanova et al., 2010), were downregulated in *RB1*$^{-/-}$ clones (Figure 1D). Despite these transcriptional changes, *RB1*$^{-/-}$ cells did not exhibit an aberrant cell cycle or differences in cell proliferation rates (Figures S1D and S1E).

Global gene expression principal component analysis revealed that 15 genes transcribed within the mitochondria contributed dramatically to the separation between control and *RB1*$^{-/-}$ clones (Figure S1F). Indeed, *RB1*$^{-/-}$ clones exhibited a significant mitochondrial gene expression

reduction (22%–58% decrease), originating from both chains of mtDNA (Figure 2A). This phenomenon can originate from depletion in the number of mitochondria or from mitochondrial malfunction. Thus, different assays were used to address these possibilities. mtDNA abundance was evaluated by calculating the ratio between mitochondrial and nuclear DNA, revealing an average depletion of 45% ± 8% ($p < 0.001$) in mtDNA in *RB1*$^{-/-}$ clones (Figure 2B). Mitochondrial function was quantified using a live-cell metabolic assay with an Agilent Seahorse analyzer. *RB1*$^{-/-}$ cells showed a 51% ± 7% ($p < 0.001$) decrease in basal respiration and a 69% ± 7% ($p < 0.001$) reduction in ATP production (the product of oxidative phosphorylation) compared with control cells. Furthermore, the maximal respiration rate of mutant cells was similarly reduced, resulting in cells respiring close to their maximal respiratory capacity (Figures 2C, S2A, and S2B). The mitochondrial respiration decrease was concomitant with a 65% ± 15% ($p < 0.001$) increase in basal cellular glycolysis and a 45% ± 7% ($p < 0.01$) increase following disruption of ATP synthesis (Figures 2C, S2A, and S2B). Calculation of glycolytic rate using a designated formula (Mookerjee et al., 2016) emphasized these differences, with mutant cells exhibiting an approximately 2-fold higher rate compared with controls (550 ± 54 and 269 + 35 pmol H^+/min/μg protein, respectively). Together, these data suggested that *RB1*$^{-/-}$ hESCs harbor a decrease in mitochondrial activity and an increase in glycolytic rate.

To evaluate any structural basis for the reduced mitochondrial activity, we visualized control and mutant cells using transmission electron microscopy (TEM) (Figures 2D and S2C). Strikingly, *RB1*$^{-/-}$ clones showed multiple phenotypes of aberrant mitochondria, such as elongated and deformed mitochondria, and ghost mitochondria. Quantification of TEM micrographs revealed a significant downregulation of normal mitochondrial hallmarks including intact outer membrane, defined cristae and adjacent ER, and an increase in mitochondria malformation (Figure 2E). Interestingly, western blot analysis did not reveal differences between inner and outer mitochondrial membrane protein expression (Figure S2D), suggesting that mitochondrial protein expression was not globally decreased and that the defect in function correlated better with mtDNA copy number (Figure 2B). Together, these data suggest that *RB1* ablation in hESCs reduces mtDNA abundance and affects mitochondrial structure and function.

hESC differentiation can shed light on developmental and malignant processes. Neural progenitor cells derived from *RB1*-null hESCs did not differ significantly from control cells (Figure S3A), suggesting that a more complex differentiation paradigm is required to model pRB's tumorigenic and developmental roles. We therefore generated teratomas from *RB1*-null and control cells, allowing us to study the effects of *RB1* ablation in vivo. Teratomas derived from *RB1*$^{-/-}$ hESCs were significantly larger than control tumors (Figures 3A and S3B). Serial sectioning of the teratomas revealed a dramatic expansion of neural structures in tumors derived from *RB1*$^{-/-}$ clones, visualized by H&E staining and immunofluorescence staining for the specific neuronal marker neural cell adhesion molecule 1 (NCAM1) (Figures 3B and 3C). RNA-seq analysis of the tumors showed a clear separation between expression patterns, with 8.0% (1,545/20,690) of the expressed transcripts at least 3-fold upregulated or downregulated in teratomas derived from *RB1*$^{-/-}$ clones (Figure S3C). In accordance with the high abundance of neural structures in the *RB1*$^{-/-}$ tumors, the upregulated genes were significantly enriched for annotations related to the nervous system and neural development (Figure 3D). Downregulated genes were enriched for epidermal related annotations, such as keratinocyte differentiation (Figure 3D). This is intriguing, as both the nervous system and the epidermis are derivatives of the same embryonic germ layer, the ectoderm. To a lesser extent, downregulated genes were enriched for muscle and bone formation categories. Interestingly, both upregulated and downregulated gene groups were enriched for transcripts annotated to include binding sites to the zinc finger E-box binding homeobox 1 (ZEB1) transcription factor (Figure 3E), which is a master regulator of the epithelial-mesenchymal transition (EMT) (Eger et al., 2005). *ZEB1* expression was previously shown to be regulated by pRB and E2F (Liu et al., 2007), and was significantly upregulated in *RB1*$^{-/-}$ teratomas (Figure 3F). Higher *ZEB1* expression correlated with epithelial and mesenchymal marker up- and downregulation, respectively (Figure 3G). ZEB1 target genes downregulated in *RB1*$^{-/-}$ teratomas included epidermal keratins, while upregulated ZEB1 target genes included neural markers such as *NCAM1* and *NCAM2*, and *NEUROD4* (Figures 3H and 3I). Furthermore, ZEB1 was previously shown to promote cell proliferation through regulation of genes such as *MKI67* and *OLIG2*, whose expression was upregulated in *RB1*$^{-/-}$ teratomas (Figure 3J). Several E2F genes were also upregulated in the mutant teratomas, correlating with enlarged tumors (Figure S3D). Finally, using immunofluorescence staining we found that *ZEB1* expression was localized to the same neural structures enlarged following *RB1* mutation, suggesting its involvement in this phenotype (Figure 3K).

Following the characterization of *RB1*-null cells and their tumorigenic capacities, we utilized them in a drug-screening platform. As TRb patients are commonly treated with chemotherapies aimed at reducing or eliminating tumors (Dunkel et al., 2010; Wright et al., 2010), we used our disease model to analyze the relative potency of a variety of chemotherapies. An initial drug screening of 119 chemotherapies approved by the Food and Drug Administration

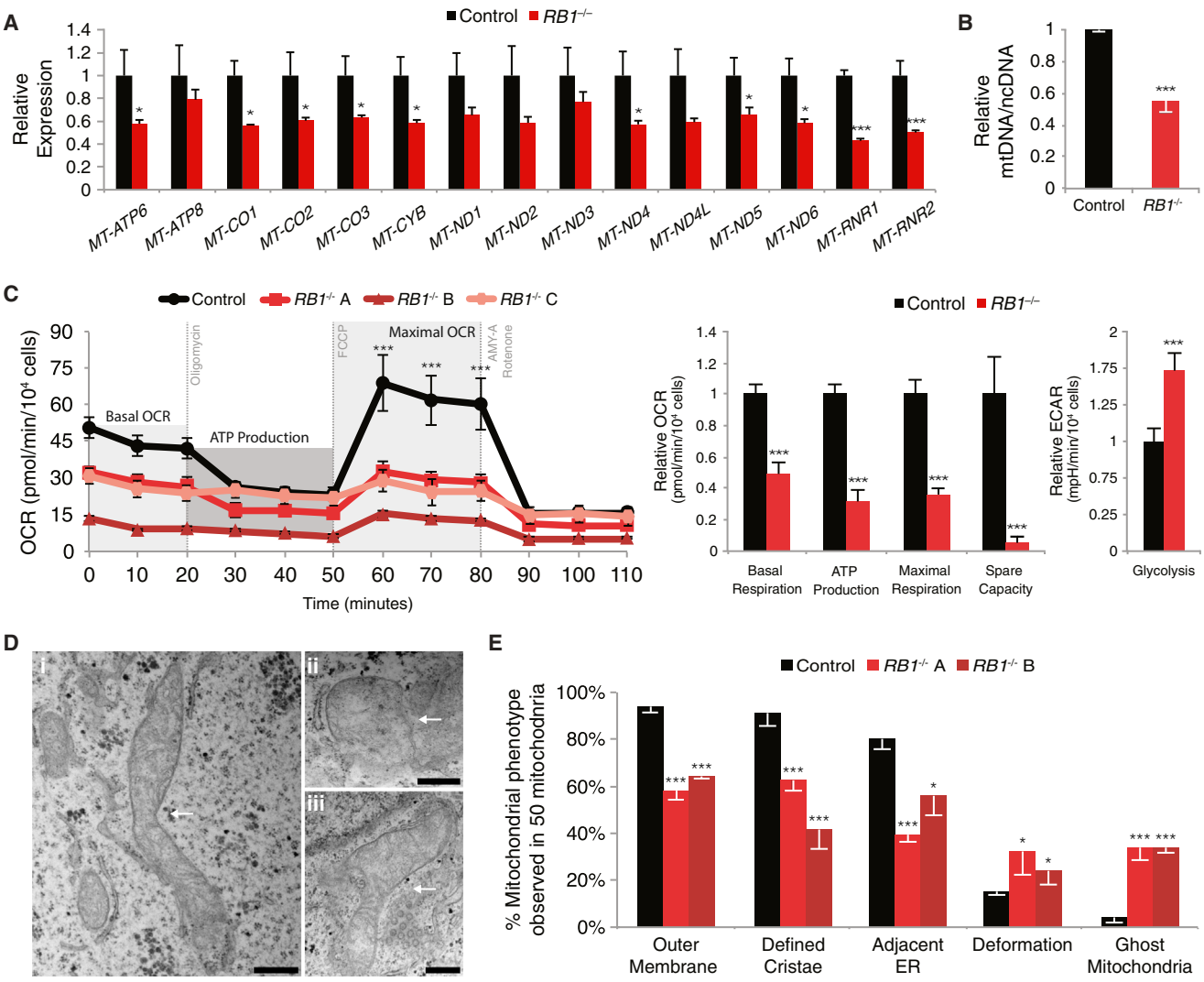

Figure 2. *RB1*$^{-/-}$ hESC Aberrant Mitochondrial Properties and Function

(A) Reduced gene expression of genes encoded from both the light and heavy chains of the mitochondrial genome in *RB1*-null hESCs. Two independent control cell lines and three mutant ones are shown.

(B) Quantification of mitochondrial DNA to nuclear DNA (mtDNA/ncDNA) ratio revealed a 45% ± 8% depletion of mtDNA in *RB1*$^{-/-}$ clones. Two independent control cell lines and three mutant ones are shown.

(C) Oxygen consumption rate (OCR) in control and *RB1*$^{-/-}$ cells following exposure to different mitochondrial stressors. Data were normalized per 10^4 cells (three independent control cell lines and three mutant ones are shown). Basal respiration was measured for 20 min, followed by oligomycin injection. At 60 min FCCP was injected, revealing significant differences in maximal respiratory capacity between control and *RB1*-null cells. Antimycin A and rotenone were injected after 80 min. Spare capacity of oxygen consumption was calculated as the difference between basal and maximal OCR. Extracellular acidification rate (ECAR), an indicator for lactate production and glycolysis, was measured for 30 min alongside basal respiration, showing a significant upregulation of glycolysis in mutant cells. FCCP, carbonyl cyanide-p-trifluoromethoxyphenylhydrazone; AMY-A, antimycin A.

(D) Representative TEM micrographs of aberrant mitochondria in *RB1*$^{-/-}$ hESCs (white arrows). Scale bars represent 1 μm.

(E) Quantification of mitochondrial aberration visualized using TEM micrographs in control and *RB1*$^{-/-}$ hESCs. Percentage of phenotypes observed out of 50 mitochondria in each cell line.

Statistical tests were performed with three independent experiments. Error bars represent SEM. *$p < 0.05$, ***$p < 0.001$ (calculated using Student's t test). See also Figure S2.

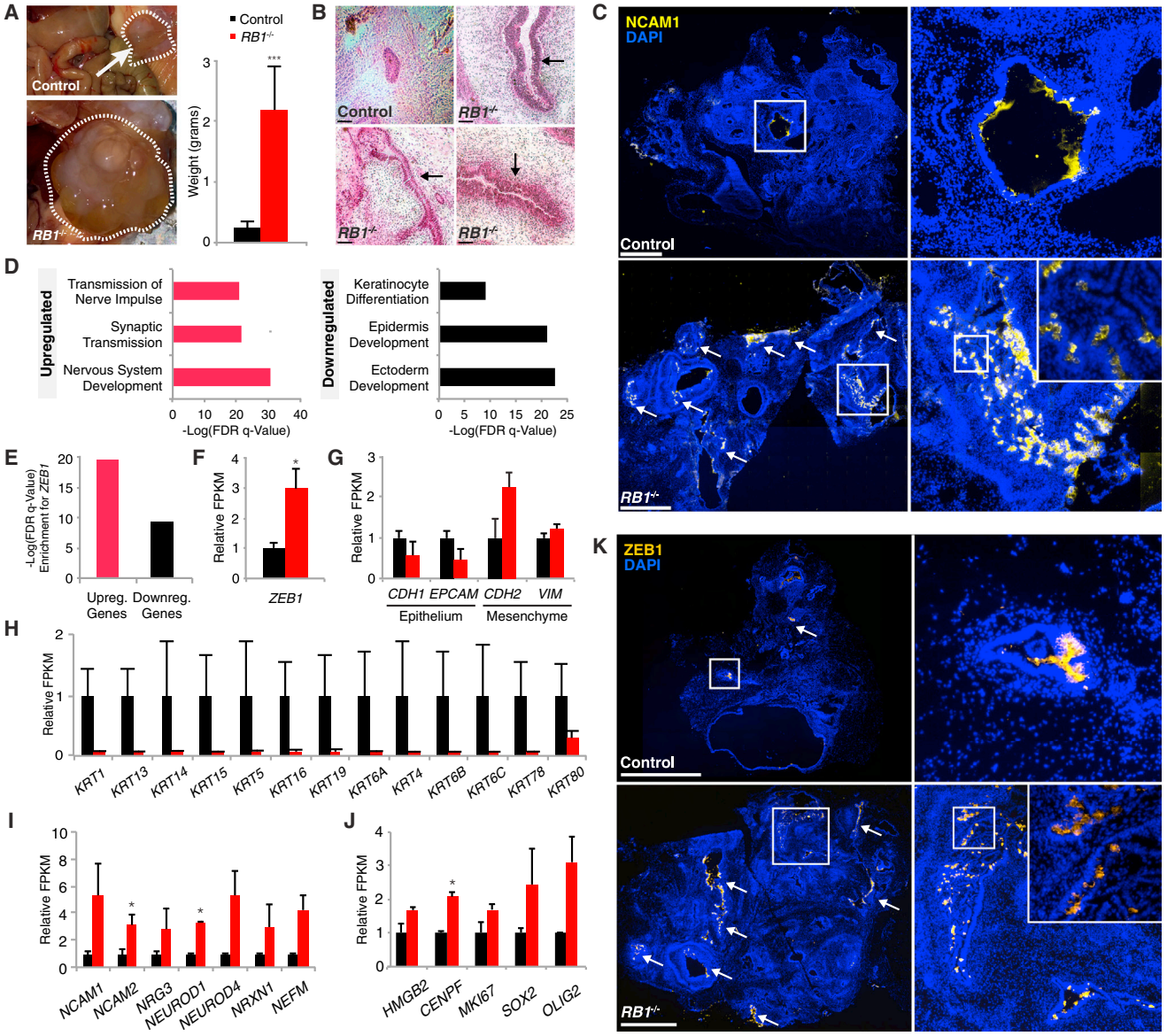

Figure 3. Analysis of *RB1*$^{-/-}$ hESC-Derived Teratomas

(A) *RB1*$^{-/-}$ hESC generate substantially larger teratomas than control cells (n = 4 control tumors, n = 12 mutant tumors). The white arrow points to a representative control teratoma.

(B) Serial sectioning and H&E staining of teratomas reveal enlarged neural structures (black arrows) in *RB1*$^{-/-}$-derived teratomas only. Scale bars represent 10 μm.

(C) Immunofluorescence staining of neural cell adhesion molecule 1 (NCAM1) (white arrows) and DAPI in control and *RB1*$^{-/-}$ teratomas. Scale bars represent 2 mm.

(D) Gene set enrichment analysis of genes up- and downregulated in *RB1*$^{-/-}$ teratomas.

(E) Significant enrichment for regulation by zinc finger E-box binding homeobox 1 (*ZEB1*) in genes up- and downregulated in *RB1*$^{-/-}$ teratomas.

(F) Relative mRNA expression of *ZEB1* in control (black) and *RB1*$^{-/-}$ teratomas (dark red).

(G) Relative mRNA expression of epithelial-mesenchymal transition markers in control (black) and *RB1*$^{-/-}$ teratomas (dark red).

(H) Relative mRNA expression of keratins suggested to be regulated by ZEB1 in control (black) and *RB1*$^{-/-}$ teratomas (dark red).

(I) Relative mRNA expression of neural markers suggested to be regulated by ZEB1 in control (black) and *RB1*$^{-/-}$ teratomas (dark red).

(legend continued on next page)

(FDA) was performed on a control and *RB1*-null cell line, with viability assessment 24, 48, and 72 hr after exposure (Figure 4A). A primary analysis was used to identify significant differential effects between the cell lines, and the effect of 12 of the chemotherapies was then analyzed on additional control and mutant cell lines (Figure 4A). The screening revealed carboplatin as a potent chemotherapy with a significant and consistent differential effect, under which the $RB1^{-/-}$ cells showed an elevated sensitivity (Figures 4B and 4C). Several chemotherapies, including carboplatin, are currently used to treat retinoblastoma, but none of the other chemotherapies showed such a specific effect on *RB1*-null cells (Figures 4B and 4C). Previous reports suggested that platinum-based chemotherapies similar to carboplatin could affect cells through mitochondrial reactive oxygen species (ROS) response (Marullo et al., 2013). Fluorescence-activated cell sorting of cells stained with mitochondrial superoxide indicator following 24 hr of exposure to carboplatin revealed that $RB1^{-/-}$ cells had significantly elevated basal levels of ROS compared with control cells (Figure 4D). Consequently, exposure to carboplatin drives ROS levels in $RB1^{-/-}$ cells dramatically higher, thus suggesting that carboplatin's specific effect on $RB1^{-/-}$ cells could originate from their deficient mitochondria. Together, these results demonstrate the potential of our model for identifying compounds specifically targeting *RB1*-null cells.

DISCUSSION

hESCs provide an extraordinary platform for disease modeling, especially for developmental disorders (Avior et al., 2016). We decided to use their unique characteristics to model developmental and tumorigenic aspects of pRB and TRb, a severe neonatal malignancy. Using gene editing, we generated heterozygous and homozygous *RB1* mutant hESCs (Figures 1A and S1). Although biallelic inactivation of *RB1* is believed to be embryonic lethal, *RB1*-null hESCs survive and proliferate normally in culture. These observations are similar to those provided by mouse models of retinoblastoma (Jacks et al., 1992). The ability of the cells to perform a normal cell cycle may originate from a functional redundancy of pRB homologous proteins, p107 and p130, encoded by the retinoblastoma-like 1 and 2 (*RBL1/2*) genes, respectively (Mulligan and Jacks, 1998). Indeed, $RB1^{-/-}$ cells showed a significant upregulation of *RBL1* expression (Figure 1C). Although such an attempt might be sufficient to maintain a normal cell cycle (Figures S1D and S1E), we found that the expression of pRB cofactors and targets is altered in *RB1*-null hESCs (Figure 1D). pRB cofactor upregulation following pRB ablation could be explained by allowing an autoregulation through positive feedback loops, as shown for E2F family members and TBX22 (Andreou et al., 2007; Johnson et al., 1994), or by ablating pRB-regulated degradation, as shown for EID1 (Miyake et al., 2000). As many pRB cofactors are transcription factors, the downstream effect of their upregulation is alterations in *RB1* target expression (Figure 1D).

The most substantial difference between control and $RB1^{-/-}$ hESCs resided in their mitochondrial properties. Mutant cells expressed lower levels of mitochondrially transcribed RNA, with a lower mtDNA copy number and a significantly aberrant mitochondrial function (Figures 2 and S2). The latter included a dramatic reduction in oxidative phosphorylation alongside an increased glycolytic rate and elevated basal levels of ROS (Figures 2C and 4D). Proliferation rate in mutant cells did not change despite the decrease in mitochondrial ATP production, probably due to an adequate compensatory increase in glycolytic ATP generation (Figures 2C and S1E). It is noteworthy that *MYC*, an E2F-pRB target upregulated in mutant cells (Figure 1D), was suggested to take part in glycolysis upregulation in naive pluripotent cells (Gu et al., 2016), and therefore could influence the observed phenotype. TEM micrographs revealed that many of the mitochondria in $RB1^{-/-}$ cells were aberrant, being either elongated, deformed, or undergoing autophagy (ghost mitochondria) (Carta et al., 2000) (Figure 2D). Similar phenotypes were recently shown to characterize poorly differentiated retinoblastoma tumor cells (Singh et al., 2016a). It is currently unknown whether these phenomena are a direct result of *RB1* biallelic inactivation. However, there have been reports of pRB localizing to the mitochondria (Ferecatu et al., 2009) and directly affecting mitochondrial-mediated apoptosis (Hilgendorf et al., 2013), perhaps mediating mitochondria biogenesis and function. Together, these data suggest the $RB1^{-/-}$ hESCs have cellular characteristics in common with retinoblastoma tumors, contributing to their use as a disease model and in drug discovery.

Utilizing hESC capabilities to differentiate toward the three embryonic germ layers, we used *RB1*-null hESCs to generate teratomas. These heterogeneous tumors are

(J) Relative mRNA expression of proliferation markers suggested to be regulated by ZEB1 in control (black) and $RB1^{-/-}$ teratomas (dark red).

(K) Immunofluorescence staining of ZEB1 (white arrows) and DAPI in control and $RB1^{-/-}$ teratomas. Scale bars represent 2 mm.

In (F) to (J), two independent control cell lines and three mutant ones are shown. Statistical tests were performed with three independent experiments. Error bars represent SEM. *p < 0.05, ***p < 0.001 (calculated using Student's t test). See also Figure S3.

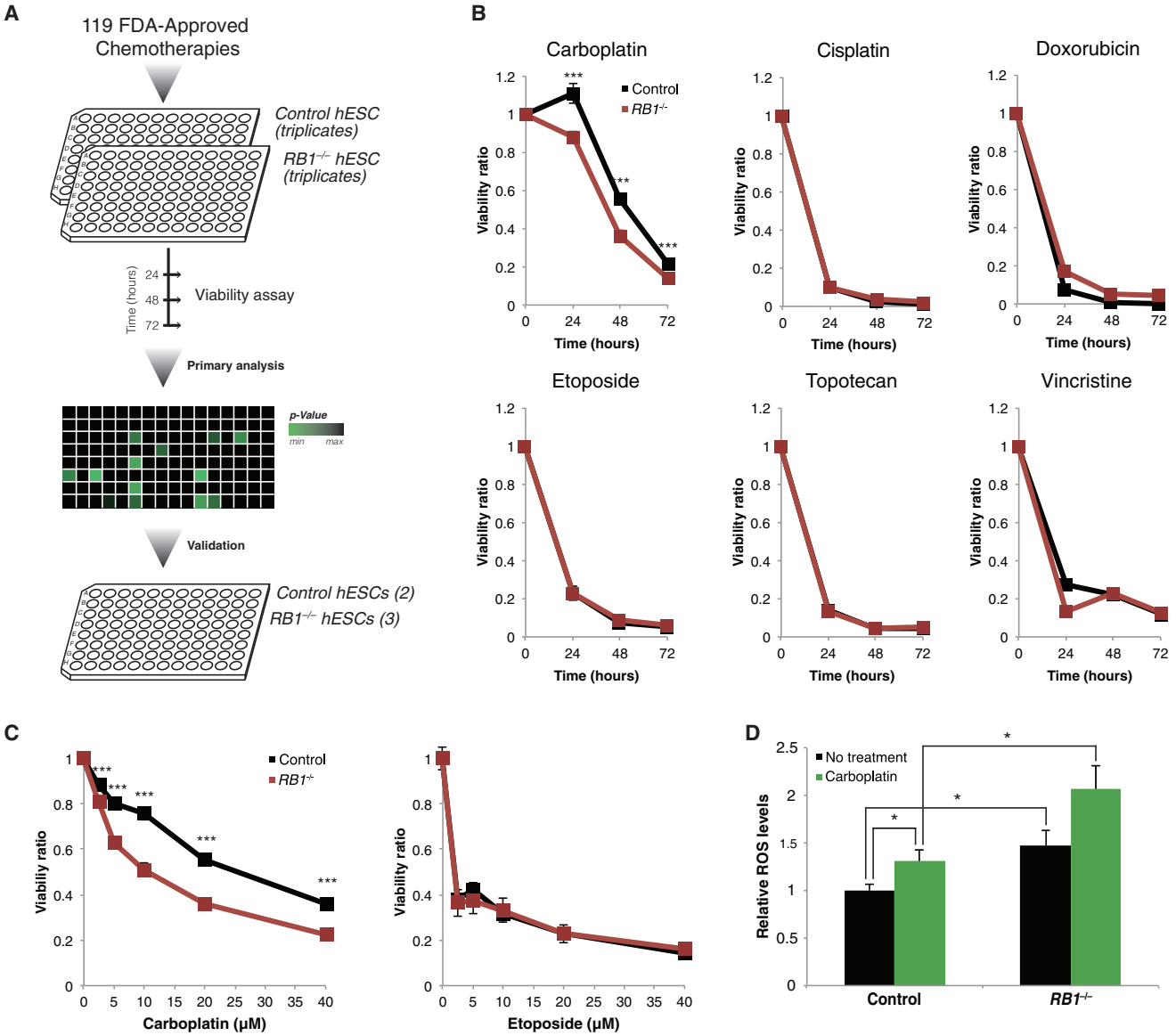

Figure 4. Differential Effects of Chemotherapies on *RB1*$^{-/-}$ Cells

(A) Schematic of experiment. A total of 119 FDA-approved chemotherapies were screened on control and *RB1*$^{-/-}$ cells, with viability evaluation after 24, 48, and 72 hr. Twelve compounds showed a statistically significant differential effect, further validated on multiple control and mutant cell lines (n = 3 experimental replicates for both control and mutant cells).

(B) Time-dependent toxicity curves of 20-μM chemotherapies commonly used to treat trilateral retinoblastoma: carboplatin, cisplatin, doxorubicin, etoposide, topotecan, and vincristine, obtained from *RB1*$^{-/-}$ (dark red) and control (black) cells (three experimental replicates for two control cell lines and three mutant ones).

(C) Dose-dependent toxicity curves of the commonly used chemotherapies, etoposide and carboplatin, obtained from *RB1*$^{-/-}$ (dark red) and control (black) cells (three experimental replicates for two control cell lines and three mutant ones).

(D) Relative levels of mitochondrial reactive oxygen species (ROS) prior and following 24-hr exposure to 10 μM carboplatin (four experimental replicates for control, three experimental replicates for *RB1*$^{-/-}$). *RB1*$^{-/-}$ cells have significantly higher basal levels of ROS, which are significantly increased following exposure to the chemotherapy.

Statistical tests were performed with three independent experiments in triplicates. Error bars represent SEM. *p < 0.02, ***p < 0.001 (calculated using Student's t test).

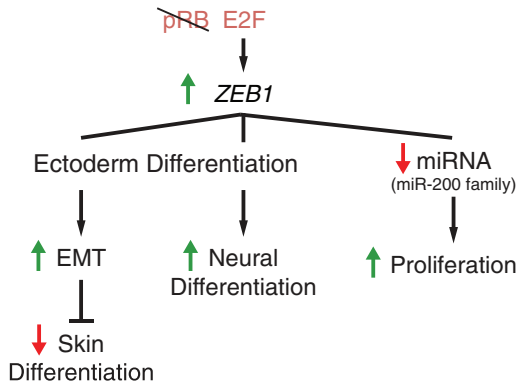

Figure 5. A Suggested Model for Effects of *RB1* Ablation on Ectodermal Differentiation and Cell Proliferation through ZEB1

Schematic model of *ZEB1*-mediated effects of *RB1* ablation on human development. Following RB1 inactivation E2F upregulates ZEB1 transcription, which in turn promotes epithelial to mesenchymal transition, causing an upregulation of neural differentiation and downregulation of keratin expression. Furthermore, ZEB1 is known to promote cell proliferation through downregulation of microRNA.

indicative of hESC tumorigenic potential and shed light on embryonic developmental processes (Avior et al., 2015; Ozolek and Castro, 2011). *RB1*-null cells generated significantly larger teratomas, suggesting that *RB1* inactivation can enhance cell proliferation alongside differentiation. Histologically, $RB1^{-/-}$ teratomas had a dramatic enhancement of neural structures (Figures 3B and 3C). The neural nature of the tumors echoes the neural component of TRb malignancy, strengthening the validity of our model.

Global gene expression of *RB1*-null teratomas revealed an upregulation of neural-related genes and a depleted expression of epidermal tissue-related genes. As both the nervous system and the epidermis originate from the ectoderm, these results suggest that the *RB1* ablation could alter early ectodermal differentiation cues. The specification between ectodermal fates occurs during early gastrulation, whereby the ventral side of the ectoderm gives rise to epidermal progenitors and the dorsal side to neural progenitors. This developmental process is mediated by repeated and extensive EMT (Duband, 2010). Genes altered in *RB1*-null teratomas were enriched for genes regulated by ZEB1, a master regulator of EMT (Figure 3E). As *ZEB1* expression is suppressed by pRB-E2F1 complex (Liu et al., 2007), inactivation of pRB promotes its expression, leading to repression of E-cadherin (Peinado et al., 2007) and a subsequent repression of epidermal markers such as keratins (Figures 3G, 3H, and 5). ZEB1 was also shown to play a key role in nervous system development in vivo (Liu et al., 2008; Singh et al., 2016b), mirrored in our model by an upregulation of its neural-related targets (Figure 3I). Together, these data provide a plausible model for the shift between two ectodermal derivatives (Figure 5). ZEB1 may also promote teratoma enlargement, as it was found to enhance proliferation (Wellner et al., 2009) and specifically regulate neural proliferation genes such as *OLIG2* and *SOX2* through microRNA repression (Siebzehnrubl et al., 2013; Wellner et al., 2009) (Figures 3J and 5). These observations are also supported by the colocalization of ZEB1 to the neural expansions in *RB1*-null derived teratomas (Figure 3K). Together, our data suggest that *RB1* developmental and tumorigenic roles could be partially mediated by *ZEB1* upregulation. Although more research is required to address these findings in vivo, it can be postulated that the embryonic lethality of *RB1* biallelic inactivation in humans originates in part from aberrant ectodermal development mediated by ZEB1.

The similarities between our model and TRb phenotypes in vivo encouraged us to use it as a drug-screening platform. While retinoblastoma is now considered a highly curable disease, TRb is responsible for more than 50% of retinoblastoma-related mortality in the United States (Broaddus et al., 2009). Chemotherapy is the preferred treatment for TRb, surpassing surgery and radiotherapy (de Jong et al., 2015), and in some cases it was enough to eradicate its symptoms (Dunkel et al., 2010; Wright et al., 2010). However, TRb remains a major challenge, with only 44%–57% 5-year survival (de Jong et al., 2015). As the effects of different chemotherapies on retinoblastoma patients vary (Lumbroso-Le Rouic et al., 2016), it is crucial to identify drugs that specifically target cells lacking *RB1*. hESCs were previously used as a platform for drug screening and discovery, facilitating a rapid transition from the bench side to the clinic (Avior et al., 2016). We tested the effects of 119 FDA-approved chemotherapies on $RB1^{-/-}$ and control cells (Figure 4A). Most of the chemotherapies, including the ones currently used to treat TRb such as etoposide and vincristine (Dunkel et al., 2010), similarly affected control and mutant cells (Figures 4B and 4C). In contrast, carboplatin, an organoplatinum compound that inhibits DNA synthesis, showed a significant, concentration-independent differential effect on *RB1*-null cells (Figure 4C). This observation of specificity is echoed in the use of carboplatin in the clinic, where it was shown to have a specific effect on retinoblastoma tumor tissues when injected into affected eyes of retinoblastoma patients, with minor effects on healthy surrounding tissues (Leng et al., 2010).

$RB1^{-/-}$ cells exhibited elevated basal levels of mitochondrial ROS compared with control cells (Figure 4D). These levels were induced in control cells following 24-hr exposure to carboplatin, while the same treatment resulted in an additional 40% increase in mitochondrial ROS levels

in *RB1* mutants (Figure 4D). Together with the mitochondrial malfunction and reduced mtDNA abundance in $RB1^{-/-}$ cells, our data suggest that *RB1*-null cells are more sensitive to carboplatin, potentially due to induced mitochondrial burden. Noticeably, the older organoplatinum chemotherapy cisplatin did not show a differential effect between control and mutant cells (Figure 4B). This can be attributed to cisplatin's elevated toxicity compared with carboplatin, rapidly eliminating all cells (Ozols et al., 2003).

It is important to note that although *RB1* inactivation is unique to retinoblastoma initiation, it is functionally inactivated in most human neoplasms (Weinberg, 1995); therefore, utilizing *RB1*-mutant cells as a drug screen platform could benefit other malignancies as well.

In conclusion, we have generated a model for TRb, a tumor-involving developmental disease, using hESCs. Undifferentiated $RB1^{-/-}$ hESCs recapitulate aspects of tumors cells, and mutant cell-derived teratomas resemble TRb tumor composition. Our model sheds light on developmental roles of *RB1* as well as on its tumorigenic effects, and can be exploited for future drug discovery.

EXPERIMENTAL PROCEDURES

Cell Culture

CSES7 and CSES9 hESCs (Biancotti et al., 2010) and their derivatives were cultured using standard conditions as previously described (Mayshar et al., 2010). See also Supplemental Experimental Procedures.

CRISPR/Cas9 Transfection and Colony Analysis

RB1 first exon sequence was obtained from the USCS Genome Browser, human genome version GRCh38/hg38. Using the Zhang laboratory online resource (http://crispr.mit.edu/) (Ran et al., 2013), two guide sequences targeting this exon were generated. Guide-carrying plasmids were created as previously described (Ran et al., 2013) using Cas9-puromycin selection plasmid (pSpCas9(BB)-2A-Puro (PX459), Addgene). See also Supplemental Experimental Procedures.

Western Blot Analysis

Western blot was performed according to standard protocols. See also Supplemental Experimental Procedures.

Karyotyping

Karyotyping was performed according to standard protocols. See also Supplemental Experimental Procedures.

Nucleic Acid Isolation

RNA was isolated using NucleoSpin RNA Plus (Macherey-Nagel and) according to the manufacturer's instructions. DNA was isolated using a GenElute mammalian genomic DNA miniprep kit (Sigma-Aldrich) according to the manufacturer's instructions.

RNA-Seq Expression Data Production, Processing, and Analysis

Total RNA samples (200 ng to 1 μg, RNA integrity number [RIN] >9) were enriched for mRNAs by pull-down of poly(A)$^+$ RNA. RNA-seq libraries were prepared using the TruSeq RNA Library Prep Kit v2 (Illumina) according to the manufacturer's protocol and sequenced using Illumina NextSeq 500 to generate 85-bp single-end reads. Raw sequencing data were extracted to FASTQ files using SRA-Tools. For a description of processing and analysis, see Supplemental Experimental Procedures.

Growth Rate Cell-Cycle Analysis

Cell growth was measured by relative cell viability 24, 48, and 72 hr after equal plating using CellTiter-Glo Luminescent Cell Viability Assay (Promega), according to the manufacturer's instructions. Cell-cycle stage was evaluated by DNA staining using propidium iodide on methanol-fixed and RNase-treated cells, followed by cell sorting using a BD FACSAria III (BD Biosciences).

mtDNA Quantification

Mitochondrial to nuclear DNA quantification ratio was analyzed by qPCR based on a previously described method (Xing et al., 2008). In brief, mitochondrial gene *MT-ND2* abundance (forward primer: 5′-TGT TGG TTA TAC CCT TCC CGT ACT A-3′; reverse primer: 5′-CCT GCA AAG ATG GTA GAG TAG ATG A-3′) was normalized to the abundance of the nuclear gene *BECN1* (forward primer: 5′-CCC TCA TCA CAG GGC TCT CTC CA-3′; reverse primer: 5′-GGG ACT GTA GGC TGG GAA CTA TGC-3′). Analysis was performed using the CFX96 qPCR system (Bio-Rad) with KAPA SYBE FAST Universal 2× qPCR Master (KAPA Biosystems).

Oxygen Consumption Measurement and Mitochondrial Function Assessment

A Seahorse XFp analyzer (Seahorse Bioscience) was used to measure the oxygen consumption rate (OCR) of undifferentiated hESCs, according to the manufacturer's protocol. See also Supplemental Experimental Procedures.

Transmission Electron Microscopy Imaging and Quantification

TEM imaging and quantification were performed according to standard protocols. See also Supplemental Experimental Procedures.

Neural Progenitor Cell Differentiation

Differentiation was performed as previously described (Kim et al., 2010). Differentiated Neural progenitor cells were stained with NCAM1 antibody (R&D Systems) and sorted by fluorescence-activated cell sorting using a BD FACSAria III (BD Biosciences).

Teratoma Formation and Analysis

All experimental procedures in animals were approved by the ethics committee of the Hebrew University. Undifferentiated hESC colonies were trypsinized into single cells. Cells ($\sim 2 \times 10^6$) were resuspended in a mixture of 100 μL of Matrigel (Corning) and 100 μL of PBS and injected subcutaneously into a NOD-SCID

mouse. Exactly 8 weeks post injection, mice were euthanized, and resulting teratomas were extracted, weighed, and dissected. Tumors were dissected into smaller pieces from different areas. Half of the tumor was frozen and saved for H&E staining, performed as previously described (Kopper et al., 2010), while the rest was kept for RNA isolation.

Immunofluorescence Staining

Cells were fixed in 4% paraformaldehyde (Sigma-Aldrich) for 15 min at room temperature. Two 5-min PBS washes were performed to remove fixation solution. Cells were then permeabilized in blocking buffer (2% BSA in PBS + 0.25% Triton X-100) for 1 hr at room temperature. Blocking buffer was then drained and replaced with blocking buffer supplemented with primary antibodies (mouse anti-NCAM [304605, BioLegend] or goat anti-ZEB1 [sc-10570, Santa Cruz Biotechnology]), diluted 1:200. Following 1 hr at room temperature, cells were washed three times in PBS for 5 min. Secondary antibodies (Cy2 or Cy3 donkey anti-goat [Jackson ImmunoResearch Laboratories]), diluted 1:200 in blocking buffer, were then added and incubated for 1 hr at room temperature. Hoechst staining was performed using bisBenzimide H33342 trihydrochloride (Sigma-Aldrich) diluted 1:10,000 in PBS, for 2 min. Sections were visualized using an Olympus IX81 microscope.

Chemotherapy Drug Screening

Drug toxicity evaluation was based on a previously described method (Ben-David et al., 2014), with slight modifications. See also Supplemental Experimental Procedures.

Mitochondrial ROS Evaluation

hESCs were seeded at a density of 7.5×10^5 cells per well on a 1 μL/cm^2 Matrigel-coated 6-well plate. Twenty-four hours after seeding, medium was changed and half of the wells were exposed to 10 μM carboplatin. Twenty-four hours later, mitochondrial ROS evaluation was performed using MitoSOX (Thermo Fisher Scientific) as previously described (Li et al., 2011). In brief, cells were incubated with 3 μM MitoSOX for 10 min, trypsinized, and fixed with 2% paraformaldehyde. Fixed cells were filtered through a 70-μm cell strainer (Corning) and analyzed with a BD FACSAria III (BD Biosciences).

ACCESSION NUMBERS

Original RNA-seq data are accessible at the NCBI GEO database under the accession number GEO: GSE84504.

SUPPLEMENTAL INFORMATION

Supplemental Information includes Supplemental Experimental Procedures and three figures and can be found with this article online at http://dx.doi.org/10.1016/j.stemcr.2017.03.005.

AUTHOR CONTRIBUTIONS

Y.A. and N.B. conceived the study and wrote the manuscript. Y.A. preformed all of the experiments and analyzed the data. E.L. assisted in teratoma analysis and staining. D.Y. was involved in the chemotherapy drug screening and its subsequent analysis. N.B. supervised the study and secured funding.

ACKNOWLEDGMENTS

The authors would like to thank Gahl Levy for his help in mitochondria-related assays, Dr. Yael Friedman and Chava Gliksmn from the Bio-Imaging unit for their work with the transmission electron microscope, and Prof. Eran Meshorer for critically reading the manuscript. Y.A. is a Clore Fellow. N.B. is the Herbert Cohn Chair in Cancer Research. This work was partially supported by the Israel Science Foundation (grant number 269/12), by The Rosetrees Trust, and by The Azrieli Foundation.

Received: October 31, 2016
Revised: March 6, 2017
Accepted: March 7, 2017
Published: April 6, 2017

REFERENCES

Andreou, A.M., Pauws, E., Jones, M.C., Singh, M.K., Bussen, M., Doudney, K., Moore, G.E., Kispert, A., Brosens, J.J., and Stanier, P. (2007). TBX22 missense mutations found in patients with X-linked cleft palate affect DNA binding, sumoylation, and transcriptional repression. Am. J. Hum. Genet. *81*, 700–712.

Andrusiak, M.G., McClellan, K.A., Dugal-Tessier, D., Julian, L.M., Rodrigues, S.P., Park, D.S., Kennedy, T.E., and Slack, R.S. (2011). Rb/E2F regulates expression of neogenin during neuronal migration. Mol. Cell. Biol. *31*, 238–247.

Avior, Y., Biancotti, J.C.C., and Benvenisty, N. (2015). TeratoScore: assessing the differentiation potential of human pluripotent stem cells by quantitative expression analysis of teratomas. Stem Cell Rep. *4*, 967–974.

Avior, Y., Sagi, I., and Benvenisty, N. (2016). Pluripotent stem cells in disease modelling and drug discovery. Nat. Rev. Mol. Cell Biol. *17*, 170–182.

Ben-David, U., and Benvenisty, N. (2011). The tumorigenicity of human embryonic and induced pluripotent stem cells. Nat. Rev. Cancer *11*, 268–277.

Ben-David, U., Arad, G., Weissbein, U., Mandefro, B., Maimon, A., Golan-Lev, T., Narwani, K., Clark, A.T., Andrews, P.W., Benvenisty, N., and Carlos Biancotti, J. (2014). Aneuploidy induces profound changes in gene expression, proliferation and tumorigenicity of human pluripotent stem cells. Nat. Commun. *5*, 4825.

Benavente, C.A., and Dyer, M.A. (2015). Genetics and epigenetics of human retinoblastoma. Annu. Rev. Pathol. *10*, 547–562.

Biancotti, J.-C., Narwani, K., Buehler, N., Mandefro, B., Golan-Lev, T., Yanuka, O., Clark, A., Hill, D., Benvenisty, N., and Lavon, N. (2010). Human embryonic stem cells as models for aneuploid chromosomal syndromes. Stem Cells *28*, 1530–1540.

Broaddus, E., Topham, A., and Singh, A.D. (2009). Survival with retinoblastoma in the USA: 1975-2004. Br. J. Ophthalmol. *93*, 24–27.

Burkhart, D.L., and Sage, J. (2008). Cellular mechanisms of tumour suppression by the retinoblastoma gene. Nat. Rev. Cancer *8*, 671–682.

Calo, E., Quintero-Estades, J.A., Danielian, P.S., Nedelcu, S., Berman, S.D., and Lees, J.A. (2010). Rb regulates fate choice and lineage commitment in vivo. Nature *466*, 1110–1114.

Carta, A., D'Adda, T., Carrara, F., and Zeviani, M. (2000). Ultrastructural analysis of extraocular muscle in chronic progressive external ophthalmoplegia. Arch. Ophthalmol. *118*, 1441–1445.

Classon, M., and Harlow, E. (2002). The retinoblastoma tumour suppressor in development and cancer. Nat. Rev. Cancer *2*, 910–917.

Conklin, J.F., Baker, J., and Sage, J. (2012). The RB family is required for the self-renewal and survival of human embryonic stem cells. Nat. Commun. *3*, 1244.

de Jong, M.C., Kors, W.A., de Graaf, P., Castelijns, J.A., Moll, A.C., and Kivela, T. (2015). The incidence of trilateral retinoblastoma: a systematic review and meta-analysis. Am. J. Ophthalmol. *160*, 1116–1126.e5.

Dimaras, H., Kimani, K., Dimba, E.A., Gronsdahl, P., White, A., Chan, H.S., and Gallie, B.L. (2012). Retinoblastoma. Lancet *379*, 1436–1446.

Duband, J.L. (2010). Diversity in the molecular and cellular strategies of epithelium-to-mesenchyme transitions: insights from the neural crest. Cell Adh. Migr. *4*, 458–482.

Dunkel, I.J., Jubran, R.F., Gururangan, S., Chantada, G.L., Finlay, J.L., Goldman, S., Khakoo, Y., O'Brien, J.M., Orjuela, M., Rodriguez-Galindo, C., et al. (2010). Trilateral retinoblastoma: potentially curable with intensive chemotherapy. Pediatr. Blood Cancer *54*, 384–387.

Dynlacht, B.D., Flores, O., Lees, J.A., and Harlow, E. (1994). Differential regulation of E2F transactivation by cyclin/cdk2 complexes. Genes Dev. *8*, 1772–1786.

Dyson, N.J. (2016). RB1: a prototype tumor suppressor and an enigma. Genes Dev. *30*, 1492–1502.

Eger, A., Aigner, K., Sonderegger, S., Dampier, B., Oehler, S., Schreiber, M., Berx, G., Cano, A., Beug, H., and Foisner, R. (2005). DeltaEF1 is a transcriptional repressor of E-cadherin and regulates epithelial plasticity in breast cancer cells. Oncogene *24*, 2375–2385.

Ferecatu, I., Le Floch, N., Bergeaud, M., Rodríguez-Enfedaque, A., Rincheval, V., Oliver, L., Vallette, F.M., Mignotte, B., and Vayssière, J.-L. (2009). Evidence for a mitochondrial localization of the retinoblastoma protein. BMC Cell Biol. *10*, 50.

Ghanem, N., Andrusiak, M.G., Svoboda, D., Al Lafi, S.M., Julian, L.M., McClellan, K.A., De Repentigny, Y., Kothary, R., Ekker, M., Blais, A., et al. (2012). The Rb/E2F pathway modulates neurogenesis through direct regulation of the Dlx1/Dlx2 bigene cluster. J. Neurosci. *32*, 8219–8230.

Goodrich, D.W. (2006). The retinoblastoma tumor-suppressor gene, the exception that proves the rule. Oncogene *25*, 5233–5243.

Gu, W., Gaeta, X., Sahakyan, A., Chan, A.B., Hong, C.S., Kim, R., Braas, D., Plath, K., Lowry, W.E., and Christofk, H.R. (2016). Glycolytic metabolism plays a functional role in regulating human pluripotent stem cell state. Cell Stem Cell *19*, 476–490.

Hilgendorf, K.I., Leshchiner, E.S., Nedelcu, S., Maynard, M.A., Calo, E., Ianari, A., Walensky, L.D., and Lees, J.A. (2013). The retinoblastoma protein induces apoptosis directly at the mitochondria. Genes Dev. *27*, 1003–1015.

Iwanaga, R., Komori, H., Ishida, S., Okamura, N., Nakayama, K., Nakayama, K.I., and Ohtani, K. (2006). Identification of novel E2F1 target genes regulated in cell cycle-dependent and independent manners. Oncogene *25*, 1786–1798.

Jacks, T., Fazeli, A., Schmitt, E.M., Bronson, R.T., Goodell, M.A., and Weinberg, R.A. (1992). Effects of an Rb mutation in the mouse. Nature *359*, 295–300.

Johnson, D.G., Ohtani, K., and Nevins, J.R. (1994). Autoregulatory control of E2F1 expression in response to positive and negative regulators of cell cycle progression. Genes Dev. *8*, 1514–1525.

Kim, D.-S., Lee, J.S., Leem, J.W., Huh, Y.J., Kim, J.Y., Kim, H.-S., Park, I.-H., Daley, G.Q., Hwang, D.-Y., and Kim, D.-W. (2010). Robust enhancement of neural differentiation from human ES and iPS cells regardless of their innate difference in differentiation propensity. Stem Cell Rev. *6*, 270–281.

Kivela, T. (2009). The epidemiological challenge of the most frequent eye cancer: retinoblastoma, an issue of birth and death. Br. J. Ophthalmol. *93*, 1129–1131.

Kopper, O., Giladi, O., Golan-Lev, T., and Benvenisty, N. (2010). Characterization of gastrulation-stage progenitor cells and their inhibitory crosstalk in human embryoid bodies. Stem Cells *28*, 75–83.

Koziczak, M., Krek, W., and Nagamine, Y. (2000). Pocket protein-independent repression of urokinase-type plasminogen activator and plasminogen activator inhibitor 1 gene expression by E2F1. Mol. Cell. Biol. *20*, 2014–2022.

Leng, T., Cebulla, C.M., Schefler, A.C., and Murray, T.G. (2010). Focal periocular carboplatin chemotherapy avoids systemic chemotherapy for unilateral, progressive retinoblastoma. Retina *30*, S66–S68.

Li, R., Jen, N., Yu, F., and Hsiai, T.K. (2011). Assessing mitochondrial redox status by flow cytometric methods: vascular response to fluid shear stress. Curr. Protoc. Cytom. *Chapter 9*, Unit9.37.

Liu, Y., Costantino, M.E., Montoya-Durango, D., Higashi, Y., Darling, D.S., and Dean, D.C. (2007). The zinc finger transcription factor ZFHX1A is linked to cell proliferation by Rb-E2F1. Biochem. J. *408*, 79–85.

Liu, Y., El-Naggar, S., Darling, D.S., Higashi, Y., and Dean, D.C. (2008). Zeb1 links epithelial-mesenchymal transition and cellular senescence. Development *135*, 579–588.

Lumbroso-Le Rouic, L., Aerts, I., Hajage, D., Lévy-Gabriel, C., Savignoni, A., Algret, N., Cassoux, N., Bertozzi, A.-I., Esteve, M., Doz, F., and Desjardins, L. (2016). Conservative treatment of retinoblastoma: a prospective phase II randomized trial of neoadjuvant chemotherapy followed by local treatments and chemothermotherapy. Eye (Lond) *30*, 46–52.

Manning, A.L., and Dyson, N.J. (2012). RB: mitotic implications of a tumour suppressor. Nat. Rev. Cancer *12*, 220–226.

Manning, A.L., Longworth, M.S., and Dyson, N.J. (2010). Loss of pRB causes centromere dysfunction and chromosomal instability. Genes Dev. *24*, 1364–1376.

Marullo, R., Werner, E., Degtyareva, N., Moore, B., Altavilla, G., Ramalingam, S.S., and Doetsch, P.W. (2013). Cisplatin induces a

mitochondrial-ROS response that contributes to cytotoxicity depending on mitochondrial redox status and bioenergetic functions. PLoS One *8*, e81162.

Mayshar, Y., Ben-David, U., Lavon, N., Biancotti, J.-C., Yakir, B., Clark, A.T., Plath, K., Lowry, W.E., and Benvenisty, N. (2010). Identification and classification of chromosomal aberrations in human induced pluripotent stem cells. Cell Stem Cell *7*, 521–531.

Merdzhanova, G., Gout, S., Keramidas, M., Edmond, V., Coll, J.L., Brambilla, C., Brambilla, E., Gazzeri, S., and Eymin, B. (2010). The transcription factor E2F1 and the SR protein SC35 control the ratio of pro-angiogenic versus antiangiogenic isoforms of vascular endothelial growth factor-A to inhibit neovascularization in vivo. Oncogene *29*, 5392–5403.

Mitter, D., Ullmann, R., Muradyan, A., Klein-Hitpass, L., Kanber, D., Ounap, K., Kaulisch, M., and Lohmann, D. (2011). Genotype-phenotype correlations in patients with retinoblastoma and interstitial 13q deletions. Eur. J. Hum. Genet. *19*, 947–958.

Miyake, S., Sellers, W.R., Safran, M., Li, X., Zhao, W., Grossman, S.R., Gan, J., DeCaprio, J.A., Adams, P.D., and Kaelin, W.G. (2000). Cells degrade a novel inhibitor of differentiation with E1A-like properties upon exiting the cell cycle. Mol. Cell. Biol. *20*, 8889–8902.

Mookerjee, S.A., Nicholls, D.G., and Brand, M.D. (2016). Determining maximum glycolytic capacity using extracellular flux measurements. PLoS One *11*, e0152016.

Mulligan, G., and Jacks, T. (1998). The retinoblastoma gene family: cousins with overlapping interests. Trends Genet. *14*, 223–229.

Ozolek, J.A., and Castro, C.A. (2011). Teratomas derived from embryonic stem cells as models for embryonic development, disease, and tumorigenesis. In Embryonic Stem Cells—Basic Biology to Bioengineering, M. Kallos, ed. (InTech) http://dx.doi.org/10.5772/23866.

Ozols, R.F., Bundy, B.N., Greer, B.E., Fowler, J.M., Clarke-Pearson, D., Burger, R.A., Mannel, R.S., DeGeest, K., Hartenbach, E.M., Baergen, R., and Gynecologic Oncology Group. (2003). Phase III trial of carboplatin and paclitaxel compared with cisplatin and paclitaxel in patients with optimally resected stage III ovarian cancer: a Gynecologic Oncology Group study. J. Clin. Oncol. *21*, 3194–3200.

Peinado, H., Olmeda, D., and Cano, A. (2007). Snail, Zeb and bHLH factors in tumour progression: an alliance against the epithelial phenotype? Nat. Rev. Cancer *7*, 415–428.

Prost, S., Lu, P., Caldwell, H., and Harrison, D. (2007). E2F regulates DDB2: consequences for DNA repair in Rb-deficient cells. Oncogene *26*, 3572–3581.

Ran, F.A., Hsu, P.D., Wright, J., Agarwala, V., Scott, D.A., and Zhang, F. (2013). Genome engineering using the CRISPR-Cas9 system. Nat. Protoc. *8*, 2281–2308.

Richter, S., Vandezande, K., Chen, N., Zhang, K., Sutherland, J., Anderson, J., Han, L., Panton, R., Branco, P., and Gallie, B. (2003). Sensitive and efficient detection of RB1 gene mutations enhances care for families with retinoblastoma. Am. J. Hum. Genet. *72*, 253–269.

Rodjan, F., de Graaf, P., Moll, A.C., Imhof, S.M., Verbeke, J.I.M.L., Sanchez, E., and Castelijns, J.A. (2010). Brain abnormalities on MR imaging in patients with retinoblastoma. AJNR Am. J. Neuroradiol. *31*, 1385–1389.

Siebzehnrubl, F.A., Silver, D.J., Tugertimur, B., Deleyrolle, L.P., Siebzehnrubl, D., Sarkisian, M.R., Devers, K.G., Yachnis, A.T., Kupper, M.D., Neal, D., et al. (2013). The ZEB1 pathway links glioblastoma initiation, invasion and chemoresistance. EMBO Mol. Med. *5*, 1196–1212.

Singh, L., Nag, T.C., and Kashyap, S. (2016a). Ultrastructural changes of mitochondria in human retinoblastoma: correlation with tumor differentiation and invasiveness. Tumor Biol. *37*, 5797–5803.

Singh, S., Howell, D., Trivedi, N., Kessler, K., Ong, T., Rosmaninho, P., Raposo, A.A., Robinson, G., Roussel, M.F., Castro, D.S., and Solecki, D.J. (2016b). Zeb1 controls neuron differentiation and germinal zone exit by a mesenchymal-epithelial-like transition. Elife *5*, e12717.

Stanelle, J., Stiewe, T., Theseling, C.C., Peter, M., and Pützer, B.M. (2002). Gene expression changes in response to E2F1 activation. Nucleic Acids Res. *30*, 1859–1867.

Thomas, D.M., Yang, H.-S., Alexander, K., and Hinds, P.W. (2003). Role of the retinoblastoma protein in differentiation and senescence. Cancer Biol. Ther. *2*, 124–130.

Vance, K.W., Shaw, H.M., Rodriguez, M., Ott, S., and Goding, C.R. (2010). The retinoblastoma protein modulates Tbx2 functional specificity. Mol. Biol. Cell *21*, 2770–2779.

Weinberg, R.A. (1995). The retinoblastoma protein and cell cycle control. Cell *81*, 323–330.

Wellner, U., Schubert, J., Burk, U.C., Schmalhofer, O., Zhu, F., Sonntag, A., Waldvogel, B., Vannier, C., Darling, D., zur Hausen, A., et al. (2009). The EMT-activator ZEB1 promotes tumorigenicity by repressing stemness-inhibiting microRNAs. Nat. Cell Biol. *11*, 1487–1495.

Wright, K.D., Qaddoumi, I., Patay, Z., Gajjar, A., Wilson, M.W., and Rodriguez-Galindo, C. (2010). Successful treatment of early detected trilateral retinoblastoma using standard infant brain tumor therapy. Pediatr. Blood Cancer *55*, 570–572.

Xing, J., Chen, M., Wood, C.G., Lin, J., Spitz, M.R., Ma, J., Amos, C.I., Shields, P.G., Benowitz, N.L., Gu, J., et al. (2008). Mitochondrial DNA content: its genetic heritability and association with renal cell carcinoma. J. Natl. Cancer Inst. *100*, 1104–1112.